AGU PUBLICATIONS

Water Resources Research

RESEARCH ARTICLE
10.1002/2014WR015643

Derivation of lowland riparian wetland deposit architecture using geophysical image analysis and interface detection

J. E. Chambers[1], P. B. Wilkinson[1], S. Uhlemann[1,2], J. P. R. Sorensen[3], C. Roberts[4], A. J. Newell[3], W. O. C. Ward[1,5], A. Binley[6], P. J. Williams[3], D. C. Gooddy[3], G. Old[4], and L. Bai[5]

[1]Geophysical Tomography Team, British Geological Survey, Nottingham, UK, [2]ETH-Swiss Federal Institute of Technology, Institute of Geophysics, Zurich, Switzerland, [3]Groundwater Science, British Geological Survey, Wallingford, UK, [4]Centre for Ecology and Hydrology, Wallingford, UK, [5]School of Computer Science, University of Nottingham, Nottingham, UK, [6]Lancaster Environment Centre, Lancaster University, Lancaster, UK

Key Points:
- Subsurface wetland architecture is characterized using 3-D resistivity imaging
- Edge detectors for resistivity image analysis are compared
- Resistivity models illuminate structures relevant to hydrological functioning

Correspondence to:
J. E. Chambers,
jonathan.chambers@bgs.ac.uk

Citation:
Chambers, J. E., et al. (2014), Derivation of lowland riparian wetland deposit architecture using geophysical image analysis and interface detection, *Water Resour. Res.*, *50*, 5886–5905, doi:10.1002/2014WR015643.

Received 3 APR 2014
Accepted 26 JUN 2014
Accepted article online 30 JUN 2014
Published online 16 JUL 2014

Abstract For groundwater-surface water interactions to be understood in complex wetland settings, the architecture of the underlying deposits requires investigation at a spatial resolution sufficient to characterize significant hydraulic pathways. Discrete intrusive sampling using conventional approaches provides insufficient sample density and can be difficult to deploy on soft ground. Here a noninvasive geophysical imaging approach combining three-dimensional electrical resistivity tomography (ERT) and the novel application of gradient and isosurface-based edge detectors is considered as a means of illuminating wetland deposit architecture. The performance of three edge detectors were compared and evaluated against ground truth data, using a lowland riparian wetland demonstration site. Isosurface-based methods correlated well with intrusive data and were useful for defining the geometries of key geological interfaces (i.e., peat/gravels and gravels/Chalk). The use of gradient detectors approach was unsuccessful, indicating that the assumption that the steepest resistivity gradient coincides with the associated geological interface can be incorrect. These findings are relevant to the application of this approach in settings with a broadly layered geology with strata of contrasting resistivities. In addition, ERT revealed substantial structures in the gravels related to the depositional environment (i.e., braided fluvial system) and a complex distribution of low-permeability putty Chalk at the bedrock surface—with implications for preferential flow and variable exchange between river and groundwater systems. These results demonstrate that a combined approach using ERT and edge detectors can provide valuable information to support targeted monitoring and inform hydrological modeling of wetlands.

1. Introduction

Groundwater-dependent ecosystems are significant in terms of their hydrological and biogeochemical functioning and as a vital habitat with considerable biodiversity and productivity. However, these systems are particularly sensitive to environmental change [e.g., *Klove et al*., 2011], and this is acknowledged in current legislation (e.g., U.S. Clean Water Act, European Union Water Framework Directive and Habitats Directive, and the Ramsar convention) resulting in a drive to characterize their functioning and understand the requirements for their sustainable management. Specifically, establishing hydrological functioning is essential as a precursor to successful management [*Zedler*, 2000]: controlling flora [*Baldwin*, 2001], fauna [*Ausden et al*., 2001], and biogeochemical cycling [*McClain et al*., 2003].

Wetland hydrology can be notoriously spatially complex as a result of heterogeneity within the subsurface [*Holden et al*., 2002; *Holden and Burt*, 2003]. However, subsurface investigations are typically spatially restricted to a limited number of core samples [e.g., *Andersen*, 2004], given the inaccessibility of many sites due to ecological sensitivity, inundation, and/or the associated costs of drillings. Geophysical investigations provide a means of achieving spatial coverage, noninvasively, to characterize the subsurface architecture of sites in order to improve our hydrological understanding.

This study considers the use of three-dimensional (3-D) electrical resistivity tomography (ERT). Crucially, this approach has the potential to provide high-resolution volumetric subsurface information, with minimal impact to the ecosystem. ERT involves the measurement of potential differences resulting from applied currents, using arrays of electrodes at the ground surface or within boreholes; an inverse problem is then

solved to produce spatial or volumetric models of the subsurface resistivity distribution from the measured data [e.g., *Loke et al*., 2013]. It is a rapidly developing technique that is being increasingly applied to geological and hydrological investigations due to its sensitivity to a range of material and fluid properties including clay content [e.g., *Shevnin et al*., 2007], porosity [e.g., *Jackson et al*., 1978], water content [e.g., *Zhou et al*., 2001], salinity [e.g., *Singha and Gorelick*, 2006], and temperature [e.g., *Hayley et al*., 2007].

In the context of wetland investigations, ERT has only been applied in relatively few studies. Most of these studies describe the application of two-dimensional (2-D) ERT for characterizing subsurface geology [*Slater and Reeve*, 2002; *Comas et al*., 2004; *Crook et al*., 2008; *Karan et al*., 2013], salinity distribution [*Heagle et al*., 2013], and the detection of thermal anomalies associated with groundwater-surface water interactions [*Musgrave and Binley*, 2011].

Far fewer wetland studies deal with the use of 3-D ERT, perhaps due to the greater difficulty of survey design, execution, and data processing. However, 3-D ERT is clearly the more appropriate method for the characterization of complex geologies, for which the 2-D assumption is violated, resulting in significant inaccuracies in 2-D ERT models [e.g., *Chambers et al*., 2002; *Loke et al*., 2013]. *Mansoor and Slater* [2007] applied on-water 3-D ERT to the investigation of a shallow water wetland (Kearney Freshwater Marsh, USA), where the resistivity structure of the wetlands sediments was illuminated and used to identify pollution pathways from local landfills. *Riddell et al*. [2010] deployed 3-D ERT surveys to develop a conceptual model of wetland forming processes in an upland setting (Manalana, South Africa). ERT was shown to be particularly effective in revealing the distribution of clay plugs within the broader sandy deposit, which exerted a major control on the hydrological functioning of the wetland. To date, there are no studies exploring the use of 3-D ERT for subsurface characterization in lowland riparian wetlands.

Emerging theoretical developments in the analysis of ERT images are also highly relevant to this study. In particular, it is postulated that automated approaches to extracting interfaces from 3-D ERT images [e.g., *Chambers et al*., 2012; *Ward et al*., 2014] will be valuable for delineating key interfaces within the subsurface. However, there are very few studies for which automated edge detection has been validated in field settings with good ground truth. In this case, where spatially dense probe data has defined the thickness of the surficial peat and alluvium deposits, the opportunity exists to quantitatively assess the performance of edge detectors for the characterization of broadly layered geological structure.

The aim is therefore to apply for the first time the latest developments in 3-D ERT image analysis to improve our understanding of the subsurface architecture of lowland riparian wetland deposits—thereby providing a foundation on which to further elucidate groundwater-surface water interactions. Specific objectives include (1) validation of image analysis approaches (derivative and isosurface methods) for interface detection using 3-D ERT against a high-resolution control data set (i.e., intrusive peat depth probing) and (2) reconstruction of the lithostratigraphic architecture of the deposits underlying the wetland, including alluvial, fluvial, and bedrock lithologies.

2. Site Description

2.1. Location and Background

The site considered here is a wetland located on the River Lambourn immediately upstream of the village of Boxford, Berkshire, UK (Figure 1). The Lambourn and its associated wetlands comprise some of the least impacted Chalk river systems in Britain, therefore providing a reference laboratory against which to compare other similar sites. The River and wetland are designated as Sites of Special Scientific Interest (SSSI) due to the habitats they provide for aquatic and terrestrial flora and fauna.

Land adjacent to the current study site has been a focus of previous research which indicated a complex geological system and hydrogeological regime [*Prior and Johnes*, 2002; *Wheater et al*., 2007; *Allen et al*., 2010; *Lapworth et al*., 2009], with the geology exerting a major control on groundwater-surface water interactions. However, the local stratigraphic and lithologic structure remains poorly understood. Promisingly, nearby 2-D ERT investigations have successfully demonstrated its use for delineating key subsurface lithologies [*Crook et al*., 2008; *Musgrave and Binley*, 2011]. Nevertheless, the challenge remains of understanding the geological complexities at the site to understand the controls on groundwater-surface water interaction without disturbing the delicate ecosystem.

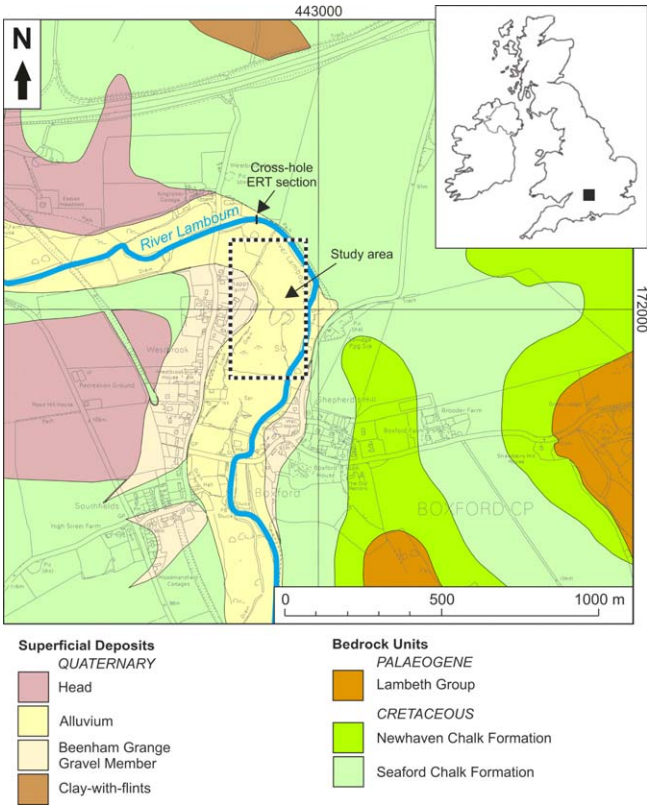

Figure 1. Geological map of Boxford and the surrounding area. Inset map (top right) shows the location of the study area at the national scale. The study area is defined by the black and white dashed line, and the location of the *Crook et al*. [2008] cross-borehole ERT survey is shown as a black line.

2.2. Geology and Geomorphology

The River Lambourn flows SE along a mostly linear valley incised into the Chalk of the Berkshire Downs (Figure 1). The Boxford site is located in the lower part of the River Lambourn at one of two conspicuous valley bends (Figure 1). The Upper Cretaceous Chalk of the Berkshire Downs is up to 252 m thick with a very shallow dip to the south east away from the steep escarpment which marks its northern boundary. The Chalk is underlain by a thin layer of Upper Greensand (Lower Cretaceous) in hydraulic continuity and sealed beneath by mudrocks of Jurassic age. A range of Quaternary and younger superficial deposits partially cover the Chalk including Clay-with-flints on interfluves and river terrace deposits, head and alluvium on valley floors [*Aldiss et al*., 2010].

At Boxford, the River Lambourn is cut into the Seaford Chalk formation (Upper Chalk), a uniform soft to medium-hard chalk with many flint nodules and a few laterally continuous tabular flints and clay-rich chalks [*Woods and Aldiss*, 2004]. The Chalk bedding dips at low angles (1–2°) across the river valley from NW to SE. Boreholes drilled at the site along the northern margin of the valley show that the River Lambourn and its floodplain is separated from the Chalk by up to 7.5 m of river terrace deposits and alluvium [*Allen et al*., 2010]. Such river terrace deposits and alluvium are common in Chalk valleys. The river terrace deposits are primarily coarse-grained gravels with typically 50% of clasts ranging from 25 to 100 mm in size. The sand, silt, and clay do not generally comprise more than 5% of the deposit, although locally thin beds of sandy gravel are developed. The gravels are typically 3–4 m thick, although there is local thickening and thinning which suggests an irregular erosion surface on the top of the Chalk. The gravels are composed predominantly of rounded flint clasts, however, the basal 1–2 m often includes a high proportion of reworked chalk material which may have been incorporated into the river terrace deposits during downcutting and erosion. The chalk clasts are often highly degraded and may have a significant hydrogeological impact by occluding porosity and significantly reducing the permeability of the gravels adjacent to the underlying chalk. In addition the upper part of the Chalk is commonly of a structureless "putty" type which has a much lower permeability than less weathered fissured Chalk [*Younger*, 1989]. In the subsequent hydrogeological discussion the term "gravels" is used to encompass the arenaceous, mainly coarse-grained, lithologies forming the river terrace deposits. The gravels are overlain by a heterogeneous cover of sands, silts, clays, peat, and tufa which are 1–2 m thick and underlie the modern floodplain surface (Figure 1). The contact with the underlying gravels is abrupt and undulating, with localized thickening of the peaty alluvial deposits in narrow, linear depressions which may result from the infill of river channels associated with the underlying gravels.

By analogy with detailed studies of the fluvial stratigraphy in downstream parts of the river system on the River Kennet [*Collins et al*., 2006], the River Lambourn and its deposits at Boxford developed in three main stages. The chalk and flint gravels which form the lower part of the valley fill were probably deposited in

high-energy bed load channels during the Late Pleistocene (Devensian) when the Berkshire Downs formed part of a periglacial environment south of the main British ice sheets [*Murton and Belshaw*, 2011]. The river hydrology was dominated by nival regimes with high spring and summer runoff [*Collins et al*., 2006] and limited water infiltration to the porous chalk bedrock because of permafrost. The high-energy rivers carved an extensive network of valleys, most of which are now dry under the modern temperate climate. Rates of weathering and erosion would have been enhanced by frost heave and brecciation [*Murton*, 1996] and the present-day linear form of the River Lambourn could indicate the importance of joints and fractures in controlling chalk weathering, erosion, and valley development [*Goudie*, 1990]. The cover of peat and alluvium accumulated in low-energy rivers and wetlands, under the temperate climate of the Holocene [*Collins et al*., 2006]. As with the present day, Chalk streams, rivers, and wetlands were probably fed primarily by groundwater supply from the Chalk aquifer. Over the last few centuries, the river and wetland at Boxford has entered its third major development stage with significant anthropogenic modification associated with the creation of a water meadow system. This involved the construction of channels and ponds for farming and recreation.

2.3. Hydrology and Hydrogeology

The water meadow would historically have been managed as pastureland. A network of channels is shown on historic maps (1882), and it is likely that these would have been used for controlled flooding or "floating" of the water meadows in the winter to protect them from frost and encourage early growth of the vegetation [e.g., *Everard*, 2005]. The site has not been grazed for a number of years, and many of the historic channels do not appear on current maps (Figure 1).

The hydrogeological functioning of the wetland is likely to depend on a number of factors. The site is located on the major Chalk aquifer, and therefore groundwater flows are likely to be important; also, the location of the wetland in a valley bottom would normally indicate a groundwater discharge zone. In addition, the River Lambourn flows through the site, potentially providing a major control on local groundwater heads as well as a focus for groundwater discharge (or recharge). However, this potentially simple valley bottom hydraulic system is made much more complex by the presence of heterogeneous river terrace gravels and wetland peat and other alluvium, and the surface water system is complicated by the presence of wetland drainage channels [*Grapes et al*., 2006].

Investigations at an adjacent riverside study site [*Allen et al*., 2010] have revealed a complex pattern of groundwater-surface water interactions, involving both influent and effluent relationships between the river and underlying gravels and with groundwater flow in the Chalk occurring under and transverse to the river. Significantly, at this study site the gravels were found to be mainly hydraulically separate from the Chalk. The study indicated that lithological knowledge was crucial to understanding the groundwater flow dynamics and the relationship between groundwater and surface water, and the same is likely to be true to an even greater degree at the adjacent wetland site, given the presence of the peat overlying the gravels. It is the complexity of the site geology and its impact on groundwater-surface water interactions that is the main driver for the 3-D geophysical characterization of the deposit structure.

3. Intrusive Methodology

The peat and alluvium depth was determined by pushing a 6 mm diameter steel rod to the contact between the penetrable peat and impenetrable gravels. This was undertaken at 2815 points with an approximate grid resolution of 5 m $\times$ 5 m (Figure 2a). The peat depth exceeded the rod length at six locations where it was assumed to be 1.86 m deep (which was the maximum depth of investigation of the metal rod). The ground level was surveyed at each point using the combination of a real-time kinematic (RTK) GPS and a Total Station.

Drilling was undertaken using a small crawler-mounted Dando Terrier percussion rig at three locations across the study site (Figure 2). Cores were recovered using a hollow stem auger in U100 tubes for logging and analysis.

4. Geophysical Methodology

4.1. ERT Survey Design and Data Collection

The 3-D ERT surveys were carried out in both the southern and northern sections of the wetland (Figure 2). A single survey covering both areas simultaneously was not possible due to the presence of significant

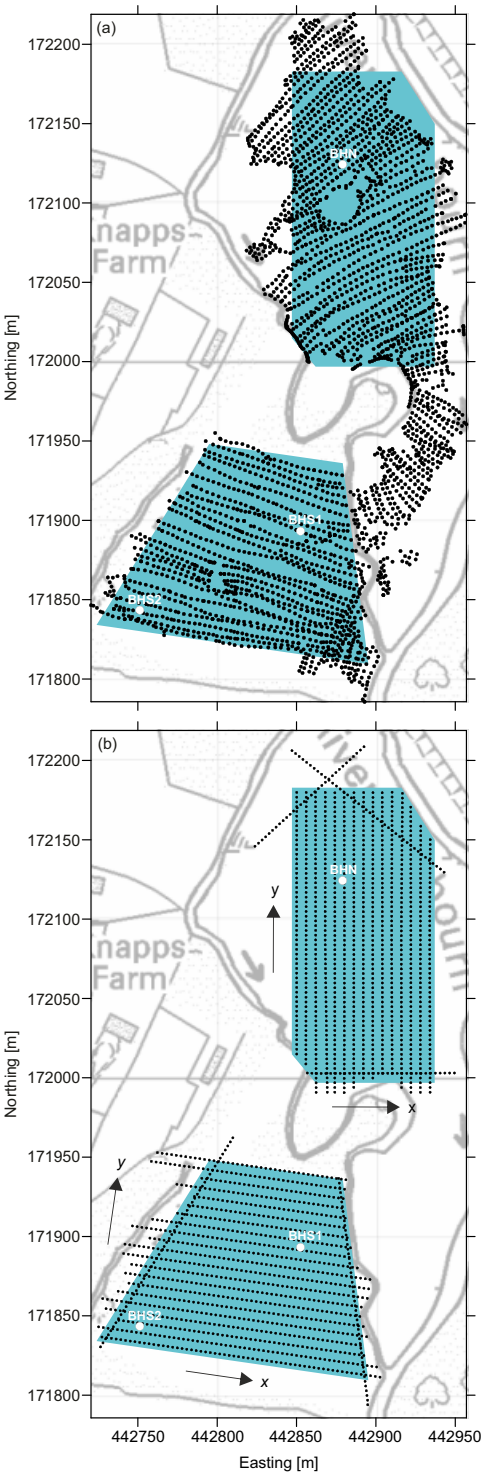

Figure 2. Annotated maps of the Boxford study site showing (a) intrusive sample locations and (b) ERT electrode positions and survey areas (blue shading).

obstructions in the central region including a stream (Figure 2) and mature vegetation. Dense vegetation prevented 3-D ERT surveys between late spring and autumn, and so the surveys were carried out in early spring (southern area) and winter (northern area) 2012, outside of the growing seasons for the sedge and other vegetation that covered much of the open areas of the wetland. Ground conditions during the survey of the southern area were good, with moist but firm ground conditions with little standing water. During the northern survey ground conditions were very soft, with shallow standing water covering much of the area.

The southern wetland survey covered an area of approximately 1.5 hectares and comprised 21 parallel survey lines, and two crosscutting lines positioned at either end of the primary survey lines with the aim of improving model resolution in low-sensitivity regions toward the edges of the model space (Figure 2b). Likewise, the northern survey extended across an area of approximately 1.6 hectares and comprised 15 parallel survey lines, with an additional three survey lines positioned at the ends of the primary survey lines, again with the aim of improving model resolution in these areas (Figure 2b). In both areas the lengths of the survey lines were constrained by site conditions, and therefore varied significantly; for the southern area lines lengths of the primary parallel lines varied from 90 to 177 m, and for the northern area between 159 and 189 m. All of the survey lines used a 3 m electrode spacing, and for the sets of primary parallel survey lines, a line spacing of 6 m. The line spacing was limited to 6 m (i.e., two along-line electrode spacings) to minimize artifacts in the resulting images associated with the use of a single line orientation [*Gharibi and Bentley*, 2005]. The dipole-dipole array was used, with dipole sizes (a) of 3, 6, 9, and 12 m and dipole separations (n) of 1a to 8a, with a

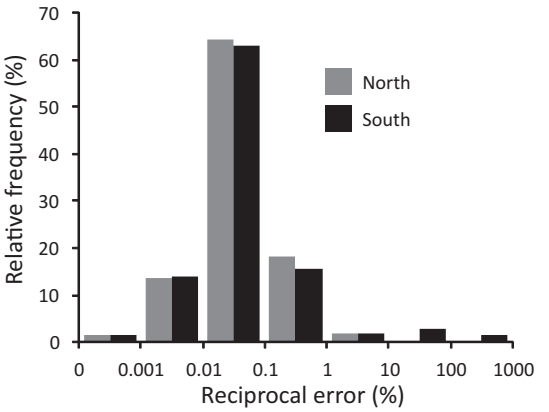

Figure 3. Distributions of reciprocal errors for the northern and southern 3-D ERT surveys.

full set of both normal and reciprocal measurements. The dipole-dipole array was chosen for good resolving capabilities, and because it effectively exploits multichannel data collection and enables efficient measurement of reciprocal combinations. Further explanation of survey design is given in Appendix A. For a normal four-electrode measurement of transfer resistance the reciprocal is found by exchanging the current and potential dipoles, and in the absence of nonlinear effects should give the same result. Reciprocal error is defined here as the percentage standard error in the average of the forward and reciprocal measurements, which provides a robust means of assessing data quality [*Binley et al*., 1996; *Wilkinson et al*., 2012]. Measurements were made using an eight-channel AGI SuperSting R8 and 64-way switch box with multicore cables attached to stainless steel rod electrodes. A maximum injection current of 500 mA was applied.

4.2. Data Processing, Inversion, and Visualization

Contact resistances averaged 395 Ω (standard deviation (SD) 130 Ω) and 292 Ω (SD 50 Ω) for the southern and northern areas, respectively. Analysis of reciprocal errors indicated very good data quality (Figure 3); 95% of the 20,563 measurement pairs (normal and reciprocal) collected during the southern area survey fell below the 5% reciprocal error (RE) threshold, while 99.5% of the 23,164 measurement pairs collected during the northern area survey had reciprocal errors falling below the 5% RE threshold. Measurements with a reciprocal error of more than 5% were removed; the remaining reciprocal pairs were averaged and the reciprocal errors were used to weight the data during the inversion. The slightly lower contact resistances, and hence slightly better reciprocal errors, observed in the northern area are probably the result of wetter ground conditions and more electrically conductive surficial deposits.

Both data sets were inverted using a regularized least squares optimization method [*Loke and Barker*, 1996]. An L2-norm was applied to the model and an L1-norm was used on the data with a cutoff factor of 0.05 [*Loke et al*., 2003; *Farquharson and Oldenburg*, 1998]. The selection of constraints is discussed in Appendix A. The forward problem was solved using a finite element method, in which node positions were adjusted to allow the observed topographic variations to be incorporated. The aim of the inversion process is to calculate a model (or image) that satisfies the observed data. A starting model is produced, i.e., a homogeneous half-space with resistivity equal to the mean of the measured apparent resistivities, for which a response is calculated and compared to the measured data. The starting model is then modified in such a way as to reduce the mean absolute misfit between the model response and the measured data. This process continues iteratively until acceptable convergence between the calculated and measured data is achieved. The resulting northern area resistivity model consisted of 45 cells in the x direction, 74 cells in the y direction, and 15 layers in the z direction, resulting in a total of 48,180 model cells; acceptable convergence was achieved after six iterations as indicated by a root mean square (RMS) misfit error of 1.03%. The southern area model comprised 61 cells in the x direction, 54 in the y direction, and 15 in the z direction, resulting in 47,700 model cell; a RMS misfit error of 1.08% was observed after five iterations.

4.3. Interface Detection

Three different methods were used to detect interfaces within the 3-D inverted ERT models. The first assumes that the interface is located at the elevation of the steepest gradient on the resistivity-elevation curve $\rho(z)$ (e.g., Figure 4) and is therefore referred to as the "steepest gradient method" (SGM) [*Chambers et al*., 2012, 2013]. Similar approaches have previously been applied to 2-D ERT images by *Nguyen et al*. [2005], *Hsu et al*. [2010], and *Bouchedda et al*. [2012]. Here the SGM uses linear interpolation of finite

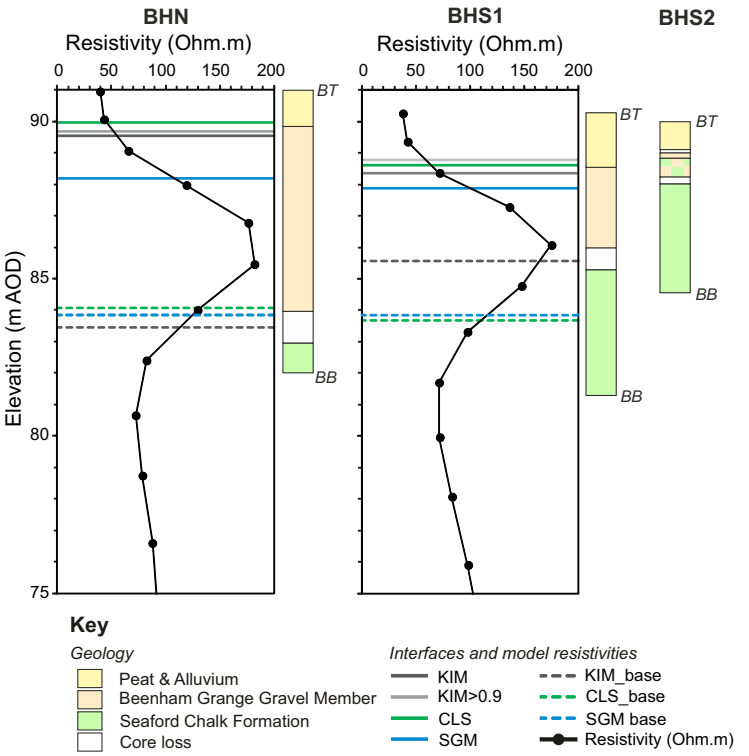

Figure 4. Resistivity data as a function of elevation, given as mAOD at surface positions corresponding to BHN and BHS1. The interfaces for the peat and alluvium/gravel and the gravel/Chalk derived using CLS, KIM, KIM > 0.9, and SGM methods are indicated. Borehole logs for BHN, BHS1, and BHS2 are shown.

difference estimates of the second derivative to find the point where $\partial^2\rho/\partial z^2 = 0$, which implicitly assumes, for simplicity, that the interfaces are close to horizontal.

The second method assumes that the interface is represented in the inverted ERT image by a resistivity isosurface. This method requires the location of the interface to be known through an independent measurement (i.e., borehole or penetration test) at one or more points in the subsurface (hence being referred to as the "known interface method," KIM). The isosurface value is then assumed to be the average of the model resistivities at those points [*Chambers et al*., 2013], and the surface is calculated by trilinear interpolation of the resistivity model $\rho(x, y, z)$. Since a single resistivity value is used to characterize a surface, this method is only applicable where a clear layered structure is present.

The third method also uses resistivity isosurfaces to identify interfaces; however, the isosurface values are determined from the statistical properties of the image rather than intrusive data. The probability distribution of resistivity values within the image is characterized using kernel density estimation, to identify distinct populations of resistivity values associated with separate units (Table 1) [*Chambers et al*., 2012]. A fuzzy *c*-means clustering method is then used to assign each cell within the image to its most likely population, thereby identifying the resistivity values that characterize the boundaries between the populations [*Ward et al*., 2014]. These values are used, as in the KIM method above, to calculate the isosurfaces representing the geological interfaces. This is referred to as the "clustering method" (CLS).

5. Results and Discussion

5.1. Surface Topography and Intrusive Investigations

Surface elevations recorded during the peat probing indicate a remarkably flat surface across the northern and southern areas with a height variation of little more than 1 m. A general increase in surface elevation to the north is observed, as is some indication of relict channel structures (particularly in the northern area) defined by sinuous linear features (Figure 5a).

Table 1. Centroid Resistivities and Interpreted Associated Lithologies for the Northern and Southern Areas Resistivity Models

Centroid Resistivity (Ωm)	Material Type
Northern Area	
35	Peat
54	Weathered chalk
98	Chalk/gravels
164	Chalk
256	Gravels
Southern Area	
49	Peat
72	Weathered chalk
102	Chalk/gravels
126	Chalk
183	Gravels

The peat forms a clear channel structure across the two survey areas. However, it is generally thicker and more extensive in the northern area (Figure 5c). The plot of peat base elevations (Figure 5b) indicates that the peat and alluvium is occupying a topographic low on the surface of the gravels.

Two of the boreholes, BHN and BHS1, were located within the peat channel in the northern and southern areas, respectively (Figure 5). Both show a substantial thickness of peat, overlying several meters of gravel, overlying chalk bedrock (Figure 4). Drilling was hampered by refusals caused by coarse material close to the interface between the gravels and chalk, which was probably related to the presence of lag deposits. BHS2 was located toward the south eastern margin of the southern area (Figures 2 and 5) and comprised approximately 1 m of peat and alluvium, overlying <0.2 m sand and gravel, a mixture of chalk and gravel (0.8 m), and chalk bedrock, which became firmer with depth. In all of the boreholes the surficial peat deposit included thin layers of clay, which was consistently observed at between 0.1 and 0.3 m below ground level. This layer was also observed in several other hand dug pits across the site.

5.2. ERT

5.2.1. Model Description

A 3-D visualization of the northern and southern ERT models is shown in Figure 6. The most electrically conductive (<50 Ωm) and resistive (>150 Ωm) values are shown as solid volumes, along with a number of vertical sections. The lithostratigraphy revealed by the boreholes is clearly displayed in the resistivity models. The most conductive materials are peat and alluvium, which span both areas in the form of a channel

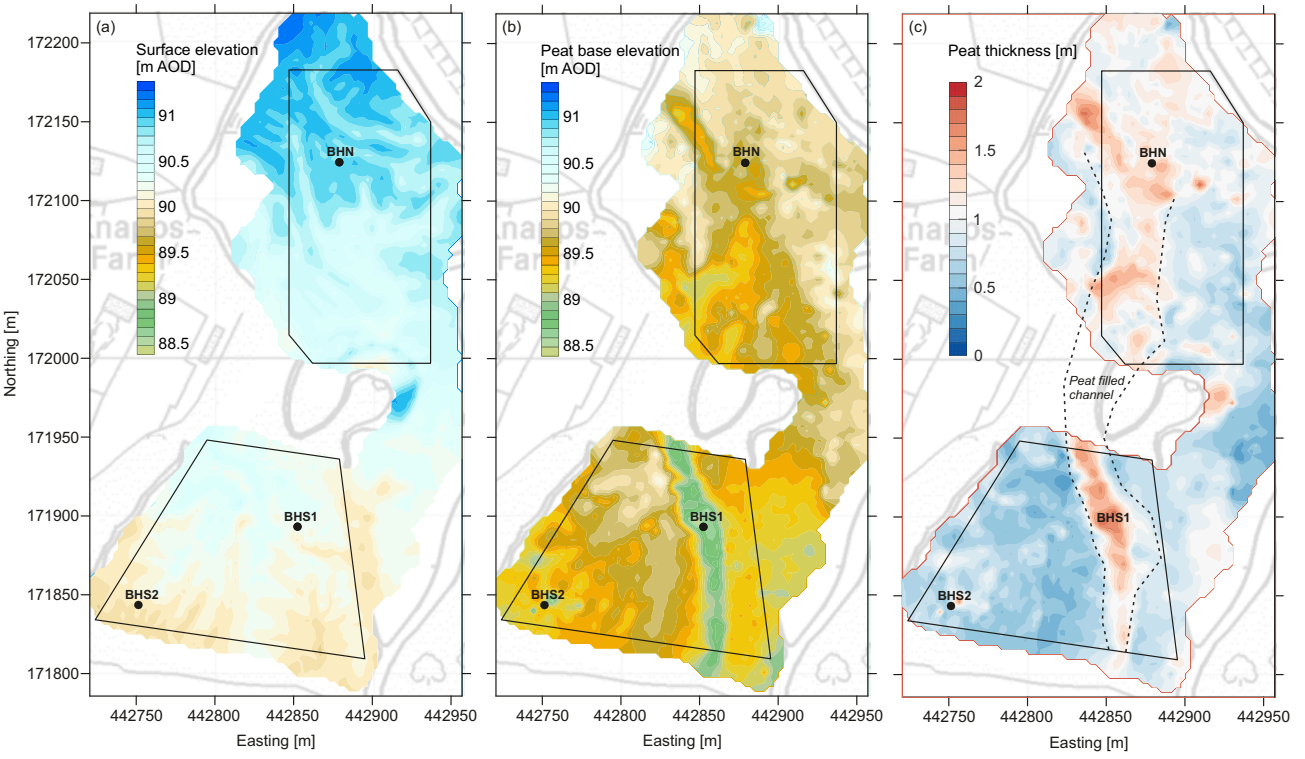

Figure 5. Boxford study site: (a) ground surface elevations derived from real-time kinematic GPS surveys and (b) peat base elevations. (c) Peat thicknesses determined from intrusive probe surveys.

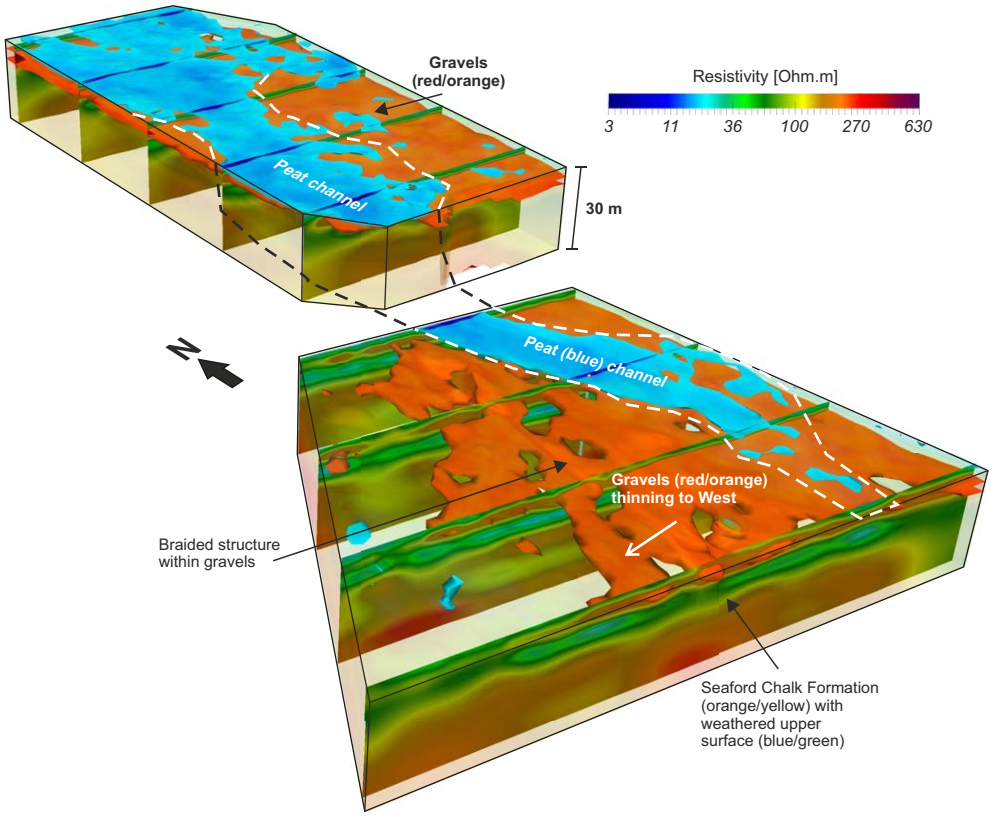

Figure 6. Three-dimensional resistivity model of the northern and southern Boxford survey areas. Solid volumes shown for resistivities of less than 50 Ωm (blues, peat) and above 150 Ωm (orange, gravels).

structure across the surface of the models, which is also consistent with the intrusive investigations. The most resistive materials are the gravels, which particularly in the southern area thin markedly to the west. This thinning can also be seen in the horizontal (Figure 7) and vertical (Figure 8) sections extracted from the 3-D model. In the south western corner of the southern area the gravels appear to be effectively absent, with peat and alluvium directly overlying chalk—an observation corroborated by BHS2 that indicates very substantial thinning of gravel in this area. The gravel also displays very significant heterogeneity, appearing to show a braided structure particularly in the western area where it thins. Chalk resistivities are intermediate between the peat and alluvium and the gravels, but display an increase in resistivity with depth (Figure 8), although this increase is highly variable and not consistent across the site.

5.2.2. Edge Detection

To determine the resistivity value for the KIM isosurface, the average resistivity value at the intrusive sample points was found by trilinear interpolation of the model resistivities at the intrusive sample points. Since the electrode spacing used in the surveys was 3 m, and the thickness of the peat was typically $<$2 m, it was uncertain whether the peat base could be resolved accurately from the resistivity models where the peat layer was thinner than one model cell. Since the top layer of model cells was 0.9 m thick, it was decided also to examine an isosurface determined by the average of the interpolated resistivity values for only those samples taken where the peat was $>$0.9 m thick (referred to as the KIM $>$ 0.9 isosurface). The results of the peat base interface detection are shown in Figure 9 for the CLS, KIM, and KIM $>$ 0.9 methods, plotted as peat thickness to aid comparisons with the probe-derived peat base data (Figure 5c). The SGM results are not shown as they consistently overestimated the depth of the interface by more than 1.2 m, indicating that the steepest gradient in the resistivity models was not located at the peat base interface. The results given in Figure 9 show the peat channel extending from north to south across the two models, with a generally broader and thicker distribution of peat in the north. There is a good degree of consistency between the CLS, KIM, and KIM $>$ 0.9 approaches, with the main difference being that the CLS method produced a thinner peat layer, particularly in the north.

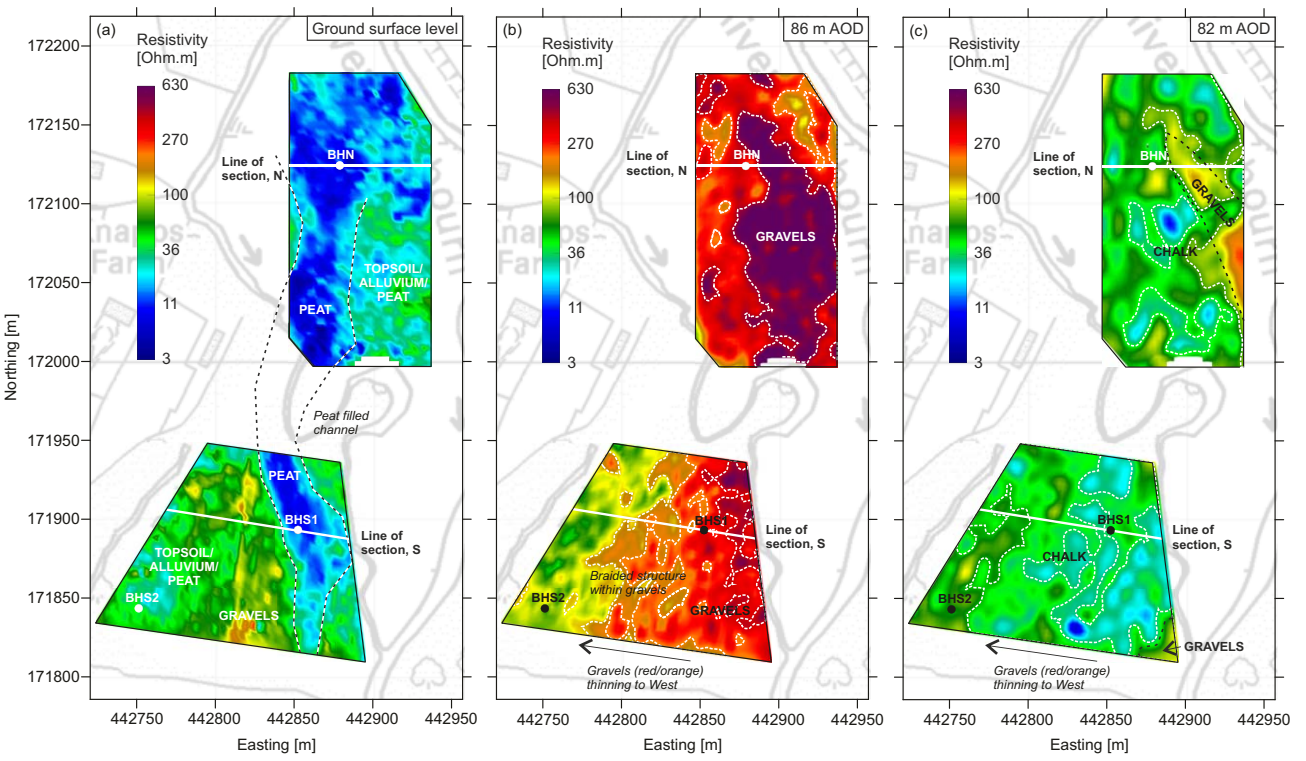

Figure 7. Horizontal sections through the 3-D resistivity models: (a) surface, (b) 86 mAOD, and (c) 82 mAOD. The black dashed lines show the interfaces between the peat and alluvium and gravels, and the gravels and Chalk. The white dashed lines indicate major braided structures within the gravels and lineations within the weathered region of the Chalk.

The interfaces recovered for the base of the gravels (or top of the chalk) are shown in Figures 9d–9f. In this case the results from the three approaches (CLS, KIM, and SGM) are generally consistent. In the north area, a clear south-eastern trending channel or scour feature can be observed on the eastern boundary. The

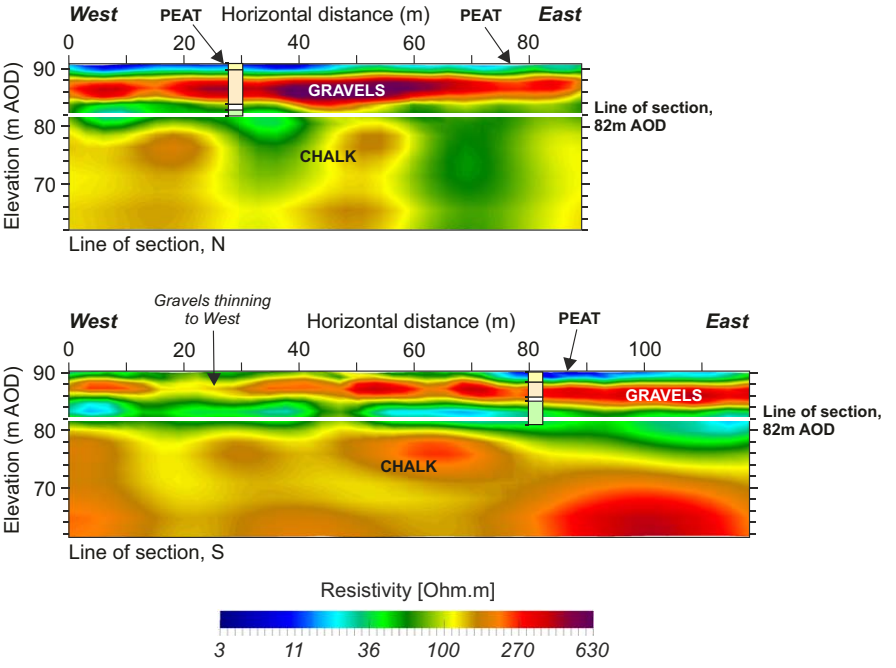

Figure 8. Vertical sections through the 3-D resistivity models: (a) north and (b) south.

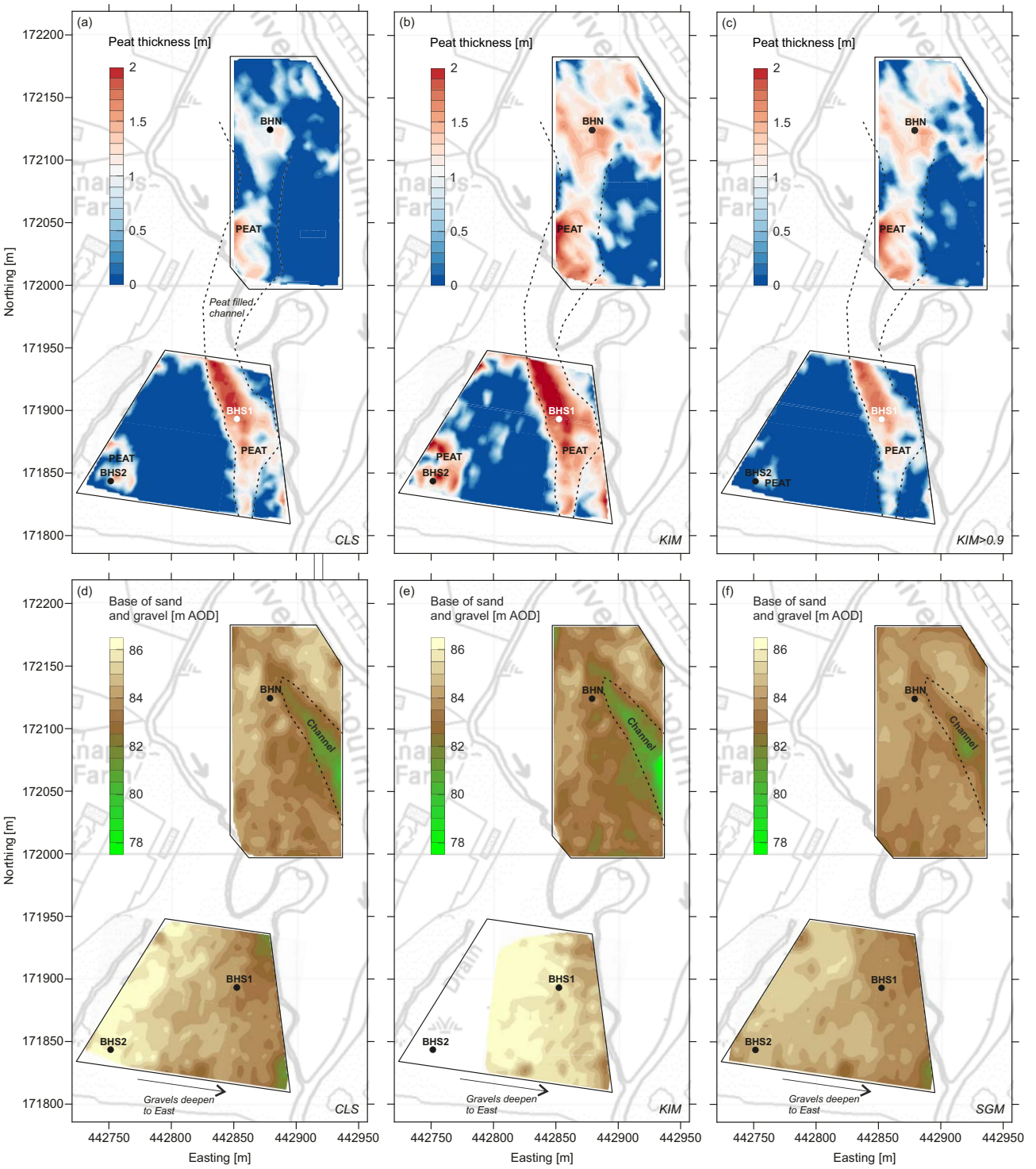

Figure 9. Peat and alluvium/gravels interface recovered using (a) CLS, (b) KIM, and (c) KIM > 0.9, and the gravel/Chalk interface recovered using (d) CLS, (e) KIM, and (f) SGM.

southern area interfaces all show the base of the gravels deepening to the east. The gravel base detected by KIM does not show the interface extending much beyond 442800mE. This is because the isosurface for the resistivity at the known interface did not extend beyond this point. This is probably due to the thinning of the gravels to the west and the failure of this approach to resolve a very thin (<1 m) gravel layer at this depth.

6. Discussion

6.1. Performance of Edge Detectors

Comparison with the intrusive probe-derived peat thickness is a useful means of assessing the performance of the edge detection algorithms. As the peat thickness probing was a direct sampling technique, it is assumed to be generally more reliable than indirect methods such as ERT, and hence constitutes a data set against which the ERT-derived edge detectors can be tested. However, it should be noted that the intrusive probing has a limitation; false depths could potentially arise due to the probe-striking coarse-grained material entrained within the peat and alluvium.

The scatter plots in Figure 10 show the correlation between the intrusive (horizontal axes) and ERT-derived peat thicknesses (vertical axes). The best fit lines are shown in green with upper and lower 95% confidence limits shown in purple and red, respectively. The thin black lines indicate the hypothetical 1:1 relationship where the ERT thickness equals the probe thickness. Eight plots are shown for each area, giving the results for the CLS, KIM, KIM $>$ 0.9, and SGM methods for two scenarios: comparison of derived thicknesses at all intrusive points (no suffix) and comparison of derived thicknesses only at points where the ERT method gave a thickness value (NZ suffix). The mean differences between the intrusively derived thickness and those determined using the CLS, KIM, and KIM $>$ 0.9 methods indicate that the ERT-based edge detectors on average underestimate peat thicknesses to a greater or lesser degree. This is because the ERT electrode spacing and measurement scheme used here, and therefore also the edge detectors, were unable to resolve the very thin surface layers of peat and alluvium. It can be seen from both Figure 9, which shows spatial plots of peat thickness, and the scatter plots in Figures 10a, 10c, 10e, 10i, 10k, and 10m, that for peat thicknesses of less than 1 m, the edge detectors tended to return a thickness of 0 m, thereby skewing the mean difference toward negative values (Table 2) and the best fits away from the 1:1 lines (Figure 10). This is shown clearly in Figure 9 where areas outside of the channel structure are characterized by an absence of peat (i.e., dark blues). This occurs because where the peat is thin there tends to be no isosurface at the derived resistivity value. Essentially the ERT survey was unable to image the peat in these regions due to the size of the electrode spacing. The correlation between the intrusive and ERT thicknesses improves if only the points where the ERT-based methods return a nonzero thickness are included (NZ suffix, Figures 10b, 10d, 10f, 10j, 10l, and 10n). When this is done, the best fits move much closer to the 1:1 lines, although in no case does it fall fully within the 95% confidence interval of the best fit (it is closest in the case of the KIM $>$ 0.9 results in the southern area). This improvement in the ERT-derived thicknesses can be seen qualitatively in Figure 9 where the areas of thicker peat ($>$1 m) correlate well with the intrusive probe-derived peat thicknesses in terms of spatial distribution and thickness.

In both areas, the SGM effectively failed to detect the peat surface with very substantial overestimates of mean peat depth of 1.28 and 1.66 m for the southern and northern areas, respectively. The steepest resistivity gradient was not coincident with the edge of the deposit, typically falling one or two model blocks below the true location of the interface. This observation is consistent with previous work [e.g., *Chambers et al*., 2013; *Hirsche et al*., 2008; *Meads et al*., 2003] where the steepest gradient in resistivity images is significantly offset from associated interface depths. It is possible to improve the results of the SGM slightly by calculating the gradients of the data on a log scale, but this only reduces the discrepancy by 0.14 m for the southern area and 0.35 m for the northern area. The likely reason for the majority of the offset is a combination of the thinness of the peat layer compared to the electrode spacing and the use of a 5 times greater damping factor in the inversion process in the uppermost model layer. The latter was applied to reduce banding effects caused by the use of parallel 2-D data electrode lines to acquire the majority of the data [*Loke et al*., 2013; *Gharibi and Bentley*, 2005]; only a few perpendicular lines were acquired due to constraints on survey time. The greater damping factor in the upper layer does not affect the KIM methods to the same extent because the isosurface is derived from the average model resistivity, which includes the effects of the damping, at the known interface points. These results emphasize the very significant challenges in using ERT to detect thin surface layers with a thickness less than that of the uppermost layer of cells of the resistivity model (which in this case was 0.9 m). In particular, the results in Figure 10 suggest that, for future analysis, reliable resolution of surface layers with a thickness of less than one third of electrode spacing should not be expected. The failure of the SGM in this case also highlights the need for intrusive data to validate and assess the geophysical results.

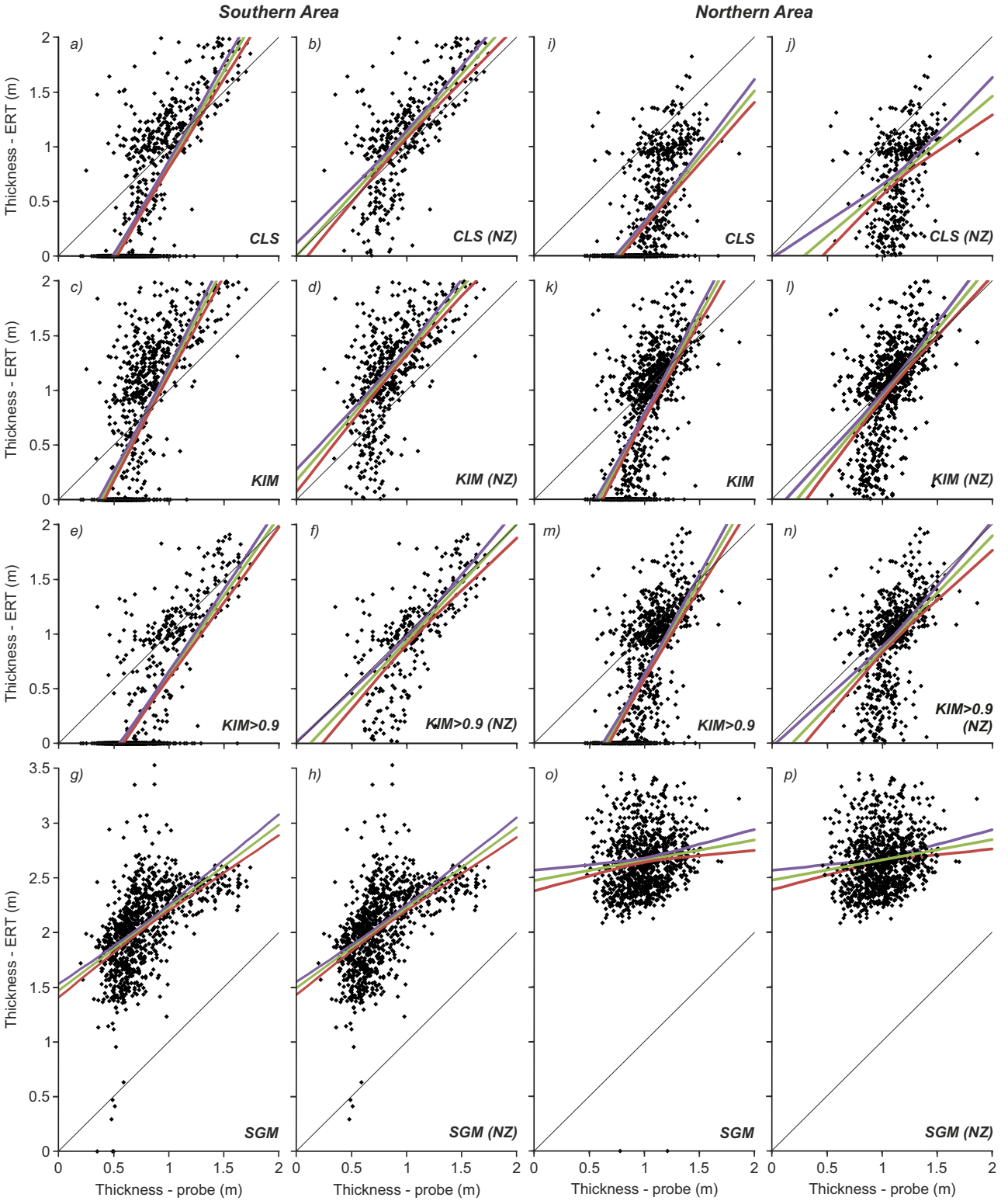

Figure 10. Scatter plots showing peat depths derived from ERT images versus intrusive probe-derived peat depths for the southern area determined using (a, b) CLS, (c, d) KIM, (e, f) KIM > 0.9, and (g, h) SGM. (i–p) Corresponding plots for the northern area. Plots with no suffix show all data, including points where a peat-alluvium/gravel interface could not be determined from the ERT-based method (thickness–ERT = 0 m). Plots with the (NZ) suffix show only data for which thickness–ERT was nonzero. Best fit and 1:1 lines are shown by green and black lines, respectively. Purple and red lines indicate upper and lower 95% confidence limits of best fits.

Table 2. Comparison Between Edge Detector and Intrusive Probe-Derived Peat Thickness

	Southern Area			Northern Area		
	Mean Difference (m)	Mean Absolute Difference (m)	RMS Difference (m)	Mean Difference (m)	Mean Absolute Difference (m)	RMS Difference (m)
CLS[a]	−0.33	0.48	0.54	−0.71	0.73	0.79
KIM[b]	−0.04	0.49	0.54	−0.24	0.40	0.51
KIM > 0.9[c]	−0.48	0.53	0.59	−0.39	0.47	0.59
SGM[d]	1.28	1.28	1.32	1.66	1.66	1.69
CLS (NZ)	0.11	0.27	0.34	−0.42	0.46	0.55
KIM (NZ)	0.33	0.42	0.50	−0.04	0.25	0.35
KIM > 0.9 (NZ)	−0.06	0.24	0.33	−0.14	0.27	0.37
SGM (NZ)	1.29	1.29	1.33	1.66	1.66	1.70

[a]Clustering.
[b]Known interface method.
[c]Known interface methods using pear depths greater than 0.9 m.
[d]Steepest gradient method.

For the deeper interface between the gravels and chalk, the geophysical edge detectors produced broadly similar results. No ground truth data, with the exception of the three boreholes, is available to assess the respective performances of the three methods. However, two factors would suggest that the KIM might be more reliable. The first is that it performed best at defining the interface between the peat and gravel, and second, it is the only approach that incorporates direct observations of the interface (i.e., the borehole used to determine the interface location) into the interpretation.

Survey design in this case was a compromise between resolution, depth of investigation, and coverage rates and was informed by the need to provide information on the deeper deposits (i.e., gravels and the top of the Chalk) as well as the peat and alluvium. Had the sole target been the peat and alluvium and their interface with the gravels, survey design would have been modified to better resolve the very near surface deposits by reducing electrode and line spacings.

6.2. Lithostratigraphy and Deposit Architecture

6.2.1. Chalk

The Chalk is represented in the model by a considerable range of resistivities, from a few tens to a few hundreds of Ωm. This variability is displayed in both the near surface and at depth. However, a strong trend of increasing resistivity with depth is observed, which is associated with the weathering of the Chalk. The variability observed in the Chalk below the weathered zone is strikingly similar to that observed by *Crook et al.* [2008] in a cross-borehole section approximately 200 m to the south west of the northern area (Figure 11) and is probably related to fracture systems and compositional changes, such as the occurrence of flints. However, Chalk in the weathered zone has been altered by brecciation [e.g., *Murton*, 1996] and the formation of clay-rich (and hence electrically conductive [e.g., *Shevnin et al.*, 2007]) putty chalk [*Younger*, 1989]. The presence of putty chalk at the site is confirmed in the boreholes. This is consistent with observations by *Crook et al.* [2008] at an adjacent site where weathered chalk, with a resistivity in the range of 10–75 Ωm, was observed during borehole investigations. The weathered chalk is seen in the northern and southern 3-D ERT models as a mantle of highly variable thickness (approximately 1–10 m) at the top of the Chalk. Although putty chalk is more commonly associated with interfluves, it has been previously observed beneath river valleys. In particular, *Younger* [1989] considers the formation of putty chalk in this setting in the Reading area of the Thames Valley in the vicinity of the study site described here. He proposes a model for its formation in periglacial conditions involving annual freeze-thaw causing pulverization of Chalk beneath minor channels leading to putty chalk formations at the gravel/Chalk interface. This would account for the highly variable nature of the putty chalk distribution, including the features in the top of the Chalk with a similar distribution and orientation to the apparent braid structures observed in the overlying gravels (Figure 7c).

6.2.2. Gravel/Chalk Interface

The gravel/Chalk interface appears to generally deepen to the north and east (~81 m AOD) (e.g., Figures 7b and 8), which is consistent with deeper scouring of the bedrock at the bend in the river where the course changes sharply from east to south. Conversely, the interface is shallowest to the southwest (~86 m AOD).

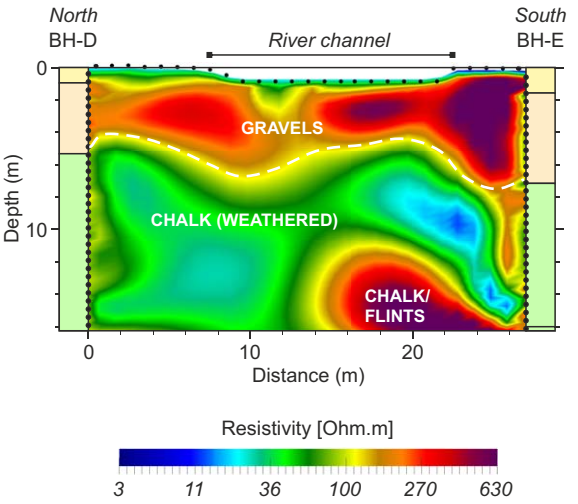

Figure 11. Cross-borehole ERT model [after *Crook et al.*, 2008]. Borehole and surface electrodes are indicated as black dots. The key for the geological logs of boreholes BH-D and BH-E is given in Figures 1 and 4. The location of the cross-hole section is shown in Figure 1.

The smaller scale lateral variability (meter to tens of meter) could indicate small-scale erosional structures or incised channels parallel and subparallel to the river course. The largest such structure can be seen on the eastern margin of the northern area, running south-southeast.

6.2.3. Gravel

The geophysical results indicate thicker and more continuous gravels in the northern area, which is closer to the present-day river course and outside of the bend in the valley where deeper scouring appears to have occurred. Again, gravel thicknesses in this area are consistent with those observed by *Crook et al.* [2008] (Figure 11). In the southern area the gravels are very much more variable and can be seen to thin markedly toward their western limits; the gravels are either very thin or absent along the western margin of the model, which is corroborated by BHS2. The gravels display a very strong internal braided or anastomosing structure, which is most apparent where they thin to the south-west of the study area. This is consistent with the terrace gravels from this region described by *Murton and Belshaw* [2011], which were up to 5 m thick, comprising sheets of sand and gravel with small-cut and fill structures in multiple channels, along with less common massive gravels that cut down through the underlying terraces deposits and, upon occasions, the bedrock.

The variability in the resistivities of the gravels will be influenced by lithological variability (i.e., variable clay content) and variations in porosity. To date intrusive sampling in the vicinity of the study area has shown that the fines content (i.e., silt and clay-sized particles) of the gravels is very low. Particle size analysis recovered from core in the north of the study area revealed fines content in the main body of the gravel to be in the range of 0.2–1%, only increasing near to the interface with the Chalk, and including the occasional thin layer of Chalk fines. Likewise, a nearby borehole (2 km down river) in the same formation described by *Gozzard* [1981] records a fines content of 2–3% in the main body of the gravels, with an increase observed to 13% within 0.6 m of the Chalk bedrock. Given the very low fines content (of which only a proportion will be clay sized), and the likelihood that the fines fraction will be predominantly Chalk-derived (and hence low activity/cation exchange capacity), it is assumed that the resistivity variations observed in the main body of the gravels are primarily a function of porosity rather than conduction on clay mineral surfaces. For the sediment types considered here it is likely that porosity will increase with both grain size and the degree of sorting [*Nelson*, 1994; *Pryor*, 1973; *Shepherd*, 1989]. *Archie* [1942] demonstrates that for saturated porous media, as porosity increases the proportion of pore fluid increases resulting in a decrease in resistivity. Consequently, well sorted and more porous gravels will display a lower resistivity than poorly sorted lower-porosity gravels. In the absence of surface conductivity, the relationship between bulk resistivity (ρ_t) and porosity (ϕ) is given as:

$$\rho_t = \phi^{-m} \rho_w$$

where m is the cementation exponent, and ρ_w is the pore fluid resistivity. For the gravels at this study site it is reasonable to assume that m = 1.5 [*Jackson et al.*, 1978, 2007]. The average pore fluid resistivity in the gravels is known to be 22 Ωm. Therefore, according to Archie, bulk resistivities of between 700 and 100 Ωm, respectively, which are very close to maximum and minimum resistivities associated with the gravels, would result in a porosity range of between 0.1 and 0.4, which is consistent with the ranges observed in

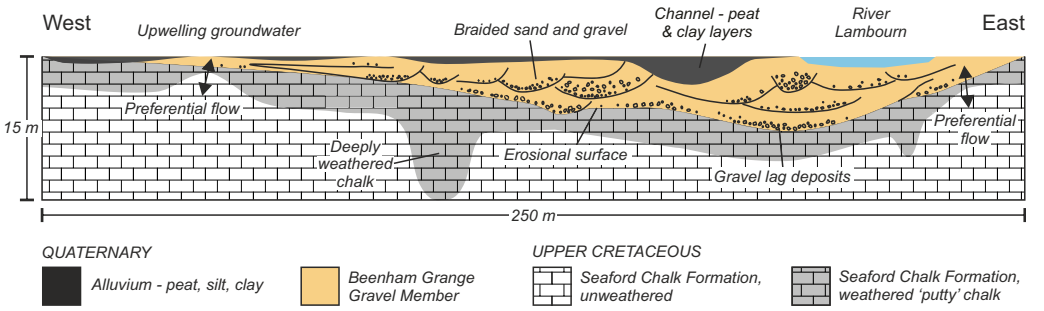

Figure 12. Schematic vertical section through the Boxford research site.

similar sedimentary settings [*Frings et al*., 2011; *Pryor*, 1973]. It is likely that the lower porosities would be associated with the finest and most poorly sorted sediments, and the highest with well-sorted gravels [*Nelson*, 1994].

6.2.4. Peat and Alluvium

The deposits of peat and alluvium cover most of the study site, as indicated by the intrusive survey, and the layer of lower resistivity observed across the top of the northern and southern resistivity models (Figure 7a). The thickest deposits occupy a channel-like structure defined by a topographic low on the surface of the gravels. Unlike the thin ($<$0.9 m) peat and alluvium in other areas of the site, these deeper channel fill deposits have been well resolved by the KIM and CLS edge detectors.

6.3. Implications for Hydrology and Hydrogeology

The distribution of low-permeability putty chalk, as indicated by the ERT surveys, aids our understanding of the potential groundwater exchange between the gravels and the Chalk. Upwelling groundwater from the Chalk bedrock into the gravels is more likely to occur where the weathered low-permeability zone is thinnest (Figure 12). This observation supports the contention of *Allen et al*. [2010] that the interaction between the gravels and underlying Chalk is highly variable. However, the variability displayed in the weathered zone of the Chalk appears to take a similar form to the braided structures seen in the gravels. This supports the model of putty chalk formation put forward by *Younger* [1989], who postulated the preferentially formation of putty chalk beneath minor channels, which in this case would be at the scale of individual channel braids. Spatial and volumetric imaging techniques such as ERT are able to spatially characterize these structures at a resolution more appropriate to the scale of heterogeneity, unlike intrusive techniques such as drilling.

The distribution of the gravels has a strong directional component (i.e., structures aligned with the direction of the water course), and given the likely relationship between resistivity distribution and porosity, and hence permeability [*Nelson*, 1994], this has significant implications for groundwater flow through the system due to directional permeability [*Pryor*, 1973]. In particular, preferential flow is likely to occur in well-sorted high-porosity units of the gravels running parallel or subparallel to the current river course, with less potential for flow perpendicular to the river.

It is also likely that the interactions between the river and the gravels will vary significantly depending on the porosity and permeability of the gravels intersecting the river, producing complex flows at a range of scales [*Allen et al*., 2010]. Again, well-sorted high-porosity and permeability gravels (hypothetically characterized by lower resistivities) are likely to provide preferential flow pathways [*Pryor*, 1973] associated with a greater degree of exchange between surface and groundwaters.

7. Conclusions

Volumetric analysis of the architecture of complex deposits underlying a lowland riparian wetland has been demonstrated using 3-D ERT. Gradient and isosurface-based edge detectors were used to automatically extract key lithostratigraphic interfaces from the resistivity models; the peat and alluvium/gravels interface and the gravels/Chalk interface. Assessment of the edge detectors was achieved with reference to a spatially dense intrusive data set of peat thickness. Three edge detectors were applied to the images, and the results

were compared with the intrusive data using the complete set of samples and the subset comprising depths greater than the thickness of the first model layer. At the 95% confidence level, there was no combination of edge detector and data set that was consistent with a 1:1 relationship between the ERT-derived and intrusively determined peat thicknesses. This implies that each ERT edge detection method exhibited a statistically significant bias with respect to the intrusive data. This bias was least for isosurfaces based on the intrusive data and was improved by restricting analysis to the subset greater than the thickness of the uppermost ERT model layer. The fuzzy clustering analysis performed slightly less well, but considerably better than the gradient-based method, which failed to correctly resolve the peat and alluvium/gravels interface even in regions of thicker peat. This was due to the peat's relative thinness compared to the electrode spacing and the need to apply greater damping to the top model layer to reduce inversion artifacts caused by the parallel 2-D data acquisition. It is likely that the resolution of the shallow peat would have been improved if a full set of orthogonal lines could have been acquired [*Gharibi and Bentley*, 2005], in which case the gradient edge detector would probably have performed better. This suggests that the fundamental assumption of SGM that the steepest gradient will be coincident with the interface must be considered carefully in light of the model discretization and inversion constraints. For a broadly layered geology with relatively homogeneous strata of contrasting resistivities, these results support previous findings [*Chambers et al*., 2013] that isosurfaces calibrated by intrusive data provide the best estimate of interface location. In the absence of intrusive data, clustering techniques may still give reasonable results. Gradient-based detectors can be useful where strata are heterogeneous [*Chambers et al*., 2012], but are unlikely to perform well in regions of the model where resolution is lower (e.g., in heavily damped areas or regions further from the electrodes).

ERT identified significant heterogeneity in terms of both thickness and internal structure of the deposits and this would not have been appreciated with necessarily more spatially restricted intrusive methods. Peat thickness varied between 0 and 2 m, with the thicker deposits occupying a channel structure across the surface of the gravels. Likewise sand and gravel thickness varied from 0 to 7 m, with upper and lower surfaces displaying significant variations in elevation. These variations along with the heterogeneity within the gravels and Chalk will have significant implications for our understanding of groundwater-surface water interactions at the site. In particular, the highly variable weathered zone at the top of the Chalk, comprising low-permeability putty chalk will exert significant controls on groundwater flows between the Chalk and gravels. Likewise, the strong directional element in the resistivity, and hence porosity, distribution of the gravels is likely to be associated with a directional permeability that will strongly influence flows through the gravels and interactions between the river and groundwater.

Three-dimensional ERT has proved to be a highly efficient approach to characterizing the geology associated with this wetland site. The resources required for the geophysical surveys were similar in terms of the field time required to the intrusive surveys, but have produced a data set with significantly richer information (i.e., a volumetric data set which reveals the architecture of the deposits underlying the wetland to a depth of approximately 25 m), which will be able to guide the development of hydrological and hydrogeological models of the site and subsequent ecological management of the site. Detailed understanding of the hydrological functioning of such complex groundwater-dependent ecosystems is essential for their management, conservation, and possible restoration and, in particular, in understanding the implications of future environmental change.

Appendix A: Survey Design and Inversion Constraints

The design of the survey had to balance the requirement for good resolution of the near surface peat deposits, which would suggest smaller electrode spacings, against the competing needs to cover the areas of interest in a reasonable time and to reconstruct the architecture of the deeper underlying deposits and bedrock, which would give a preference for larger spacings. An electrode spacing of 3 m was eventually chosen since this gave a maximum line length of 189 m with 64 electrodes and a maximum depth-of-investigation using the dipole-dipole array of ~27 m. At the same time, using the standard model discretization in the inversion code (Res3DInv, Geotomo Software, www.geotomosoft.com), this still placed 2–3 vertical model cells within the typical thickness of the peat layer.

Similarly, the constraints placed on the resistivity model during the inversion had to be carefully considered. In many circumstances an L1 model constraint [*Loke et al*., 2003] is preferred when investigating lithological

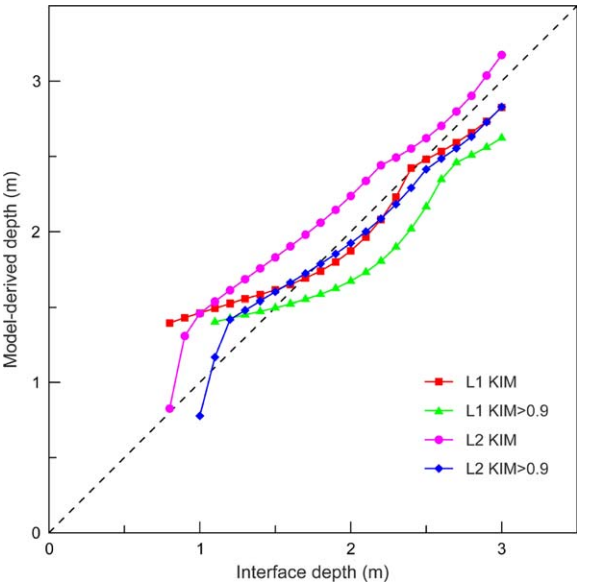

Figure A1. Model-derived depths as a function of true interface depth.

boundaries since it favors sharp changes in resistivity. But in this case, although the peat boundary was expected to be sharp, other interfaces of interest within the region (e.g., between the gravels and the chalk) had a gradational character. In addition, the use of an L1 constraint tends to align resistivity boundaries to model cell edges, which can cause unrealistic step-like changes with position when an interface is subhorizontal. This is particularly pronounced if the lithological layers being investigated are thin (such as the peat layer here). On balance, an L2 model constraint was therefore thought to provide the best compromise.

The effects of these decisions are demonstrated here using synthetic models. Data were generated for a single line of 64 electrodes spaced at 3 m using dipole-dipole configurations with a = 3, 6, 9, 12 m and n = 1–8. The forward models were one-dimensional and comprised a layer of peat between 0.1 and 3.0 m thick (in 0.1 m increments) with resistivity $\rho = 15\ \Omega$m, underlain by a layer of gravel with $\rho = 200\ \Omega$m so that the total thickness of peat and gravel was 5.0 m. This was in turn underlain by chalk bedrock with $\rho = 100\ \Omega$m. The data were inverted using Res2DInv with the same model discretization, damping factors and data constraint used in the 3-D inversions. Both L1 and L2 model constraints were applied, and results were simulated for the situations where all peat interface depths were considered (KIM) and where only interface depths greater than 0.9 m were used (KIM > 0.9).

The resistivity at the interface depth was determined for each inverted model. To reflect site conditions, a weighted average of these was calculated with the weighting taken to be the frequency with which that depth was observed in the real peat probe data set (e.g., for a modeled peat depth of 1.1 m, the proportion of peat depths observed in the range 1.05–1.15 m was 0.098). The weighted average was used as the resistivity value to determine the depth to the interface. This was calculated for the four combinations of L1 or L2 model constraints and all depths (KIM) or depths >0.9 m (KIM > 0.9). The results were L1 KIM, $\rho_{int} = 35.5\ \Omega$m; L1 KIM > 0.9, $\rho_{int} = 27.4\ \Omega$m; L2 KIM, $\rho_{int} = 37.5\ \Omega$m; L2 KIM > 0.9, $\rho_{int} = 30.7\ \Omega$m. The interface depths at these resistivity values are shown in Figure A1. The depths derived from the L1 model show a somewhat step-like dependence against the true depth, whether they were determined using the KIM or KIM > 0.9 resistivity. In contrast the L2 model depths vary more smoothly with the true depth. This is due to the effect mentioned above of the L1 constraint preferring to place the interface on model cell boundaries. The RMS errors between the model-derived and true depths were L1 KIM: 0.246 m; L1 KIM > 0.9: 0.283 m; L2 KIM: 0.276 m; L2 KIM > 0.9: 0.130 m. For the survey geometry and lithological architecture at this site, these results show that using an L2 model constraint with intrusive data only from depths greater than the first model block gives the best approximation when using isoresistivity contours to determine the peat interface location.

Acknowledgments
This paper is published with the permission of the Executive Director of the British Geological Survey (NERC). Data used to generate the resistivity models are archived by the British Geological Survey, and are available from the authors.

References

Aldiss, D. T., et al. (2010), *Geology of the Newbury District and Part of the Abingdon District*, Br. Geol. Surv., Nottingham, U. K.

Allen, D. J., W. G. Darling, D. C. Gooddy, D. J. Lapworth, A. J. Newell, A. T. Williams, D. Allen, and C. Abesser (2010), Interaction between groundwater, the hyporheic zone and a Chalk stream: A case study from the River Lambourn, UK, *Hydrogeol. J.*, *18*(5), 1125–1141, doi: 10.1007/s10040-010-0592-2.

Andersen, H. E. (2004), Hydrology and nitrogen balance of a seasonally inundated Danish floodplain wetland, *Hydrol. Processes*, *18*(3), 415–434, doi:10.1002/hyp.1277.

Archie, G. E. (1942), The electrical resistivity log as an aid in determining some reservoir characteristics, *Trans. AIME*, *146*, 54–62.
Ausden, M., W. J. Sutherland, and R. James (2001), The effects of flooding lowland wet grassland on soil macroinvertebrate prey of breeding wading birds, *J. Appl. Ecol.*, *38*(2), 320–338, doi:10.1046/j.1365-2664.2001.00600.x.
Baldwin, A. H., M. S. Egnotovich, and E. Clarke (2001), Hydrologic change and vegetation of tidal freshwater marshes: Field, greenhouse, and seed-bank experiments, *Wetlands*, *21*(4), 519–531, doi:10.1672/0277-5212(2001)021[0519:hcavot]2.0.co;2.
Binley, A., B. Shaw, and S. Henry-Poulter (1996), Flow pathways in porous media: Electrical resistance tomography and dye staining image verification, *Meas. Sci. Technol.*, *7*(3), 384–390, doi:10.1088/0957-0233/7/3/020.
Bouchedda, A., M. Chouteau, A. Binley, and B. Giroux (2012), 2-D joint structural inversion of cross-hole electrical resistance and ground penetrating radar data, *J. Appl. Geophys.*, *78*, 52–67, doi:10.1016/j.jappgeo.2011.10.009.
Chambers, J. E., R. D. Ogilvy, O. Kuras, J. C. Cripps, and P. I. Meldrum (2002), 3D electrical imaging of known targets at a controlled environmental test site, *Environ. Geol.*, *41*(6), 690–704, doi:10.1007/s00254-001-0452-4.
Chambers, J. E., et al. (2012), Bedrock detection beneath river terrace deposits using three-dimensional electrical resistivity tomography, *Geomorphology*, *177*, 17–25, doi:10.1016/j.geomorph.2012.03.034.
Chambers, J. E., P. B. Wilkinson, S. Penn, P. I. Meldrum, O. Kuras, M. H. Loke, and D. A. Gunn (2013), River terrace sand and gravel deposit reserve estimation using three-dimensional electrical resistivity tomography for bedrock surface detection, *J. Appl. Geophys.*, *93*, 25–32, doi:10.1016/j.jappgeo.2013.03.002.
Collins, P. E. F., P. Worsley, D. M. Keith-Lucas, and I. M. Fenwick (2006), Floodplain environmental change during the Younger Dryas and Holocene in Northwest Europe: Insights from the lower Kennet Valley, south central England, *Palaeogeogr. Palaeoclimatol. Palaeoecol.*, *233*(1–2), 113–133, doi:10.1016/j.palaeo.2005.09.014.
Comas, X., L. Slater, and A. Reeve (2004), Geophysical evidence for peat basin morphology and stratigraphic controls on vegetation observed in a Northern Peatland, *J. Hydrol.*, *295*(1–4), 173–184, doi:10.1016/j.jhydrol.2004303.008.
Crook, N., A. Binley, R. Knight, D. A. Robinson, J. Zarnetske, and R. Haggerty (2008), Electrical resistivity imaging of the architecture of substream sediments, *Water Resour. Res.*, *44*, W00D13, doi:10.1029/2008WR006968.
Everard, M. (2005), *Water Meadows*, 289 pp., Forrest Text, Ceredigion, U. K.
Farquharson, C. G., and D. W. Oldenburg (1998), Non-linear inversion using general measures of data misfit and model structure, *Geophys. J. Int.*, *134*(1), 213–227, doi:10.1046/j.1365-246x.1998.00555.x.
Frings, R. M., H. Schuettrumpf, and S. Vollmer (2011), Verification of porosity predictors for fluvial sand-gravel deposits, *Water Resour. Res.*, *47*, W07525, doi:10.1029/2010WR009690.
Gharibi, M., and L. R. Bentley (2005), Resolution of 3-D electrical resistivity images from inversions of 2-D orthogonal lines, *J. Environ. Eng. Geophys.*, *10*(4), 339–349, doi:10.2113/JEEG10.4.339.
Goudie, A. (1990), *The Landforms of England and Wales*, Basil Blackwell, Oxford, U. K.
Gozzard, J. R. (1981), The sand and gravel resources of the country around Newbury, Berkshire, Part 1: around Newbury, Description of 1: 25000 sheet SU46 and parts of SU36, 37 and 47 [and] Part 2: North-east of Newbury. Description of 1:25000 sheet SU57, Mineral Assessment Report 59, Institute of Geological Sciences, Her Majesty's Stationary Office (HMSO), London, U. K.
Grapes, T. R., C. Bradley, and G. E. Petts (2006), Hydrodynamics of floodplain wetlands in a chalk catchment: The River Lambourn, UK, *J. Hydrol.*, *320*(3–4), 324–341, doi:10.1016/j.jhydrol.2005.07.028.
Hayley, K., L. R. Bentley, M. Gharibi, and M. Nightingale (2007), Low temperature dependence of electrical resistivity: Implications for near surface geophysical monitoring, *Geophys. Res. Lett.*, *34*, L18402, doi:10.1029/2007GL031124.
Heagle, D., M. Hayashi, and G. van der Kamp (2013), Surface-subsurface salinity distribution and exchange in a closed-basin prairie wetland, *J. Hydrol.*, *478*, 1–14, doi:10.1016/j.jhydrol.2012.05.054.
Hirsch, M., L. R. Bentley, and P. Dietrich (2008), A comparison of electrical resistivity, ground penetrating radar and seismic refraction results at a river terrace site, *J. Environ. Eng. Geophys.*, *13*(4), 325–333, doi:10.2113/JEEG13.4.325.
Holden, J., and T. P. Burt (2003), Runoff production in blanket peat covered catchments, *Water Resour. Res.*, *39*(7), 1191, doi:10.1029/2002WR001956.
Holden, J., T. P. Burt, and M. Vilas (2002), Application of ground-penetrating radar to the identification of subsurface piping in blanket peat, *Earth Surf. Processes Landforms*, *27*(3), 235–249, doi:10.1002/esp.316.
Hsu, H. L., B. J. Yanites, C. C. Chen, and Y. G. Chen (2010), Bedrock detection using 2D electrical resistivity imaging along the Peikang River, central Taiwan, *Geomorphology*, *114*(3), 406–414, doi:10.1016/j.geomorph.2009.08.004.
Jackson, P. D., D. Taylor-Smith, and P. N. Stanford (1978), Resistivity-porosity-particle shape relationships for marine sands, *Geophysics*, *43*(6), 1250–1268, doi:10.1190/1.1440891.
Jackson, P. D., J. F. Williams, M. A. Lovell, A. Camps, C. Rochelle, and A. E. Milodowski (2007), An investigation of the exponent in Archie's equation: Comparing numerical modeling with laboratory data: Towards characterising disturbed samples from the Cascadia Margin: IODP Expedition 311, in Society of Petrophysicists and Well Log Analysts (SPWLA) 49th Annual Logging Symposium, 10 pp., SPWLA, Edinburgh.
Karan, S., P. Engesgaard, M. C. Looms, T. Laier, and J. Kazmierczak (2013), Groundwater flow and mixing in a wetland-stream system: Field study and numerical modeling, *J. Hydrol.*, *488*, 73–83, doi:10.1016/j.jhydrol.2013.02.030.
Klove, B., et al. (2011), Groundwater dependent ecosystems. Part I: Hydroecological status and trends, *Environ. Sci. Policy*, *14*(7), 770–781, doi:10.1016/j.envsci.2011.04.002.
Lapworth, D. J., D. C. Gooddy, D. Allen, and G. H. Old (2009), Understanding groundwater, surface water and hyporheic zone biogeochemical processes in a Chalk catchment using fluorescence properties of dissolved and colloidal organic matter, *J. Geophys. Res.*, *114*, G00F02, doi:10.1029/2009JG000921.
Loke, M. H., and R. D. Barker (1996), Practical techniques for 3D resistivity surveys and data inversion, *Geophys. Prospect.*, *44*(3), 499–523, doi:10.1111/j.1365-2478.1996.tb00162.x.
Loke, M. H., I. Ackworth, and T. Dahlin (2003), A comparison of smooth and blocky inversion methods in 2D electrical imaging surveys, *Explor. Geophys.*, *34*, 182–187.
Loke, M. H., J. E. Chambers, D. F. Rucker, O. Kuras, and P. B. Wilkinson (2013), Recent developments in the direct-current geoelectrical imaging method, *J. Appl. Geophys.*, *95*, 135–156, doi:10.1016/j.jappgeo.2013.02.017.
Mansoor, N., and L. Slater (2007), Aquatic electrical resistivity imaging of shallow-water wetlands, *Geophysics*, *72*(5), F211–F221, doi:10.1190/1.2750667.
McClain, M. E., et al. (2003), Biogeochemical hot spots and hot moments at the interface of terrestrial and aquatic ecosystems, *Ecosystems*, *6*, 301–312, doi:10.1007/s10021-003-0161-9.

Meads, L. N., L. R. Bentley, and C. A. Mendoza (2003), Application of electrical resistivity imaging to the development of a geologic model for a proposed Edmonton landfill site, *Canadian Geotechnical Journal*, *40*(3), 551–558, doi:10.1139/t03-017.

Murton, J. B. (1996), Near-surface brecciation of chalk, Isle of Thanet, south-east England: A comparison with ice-rich brecciated bedrocks in Canada and Spitsbergen, *Permafrost Periglacial Processes*, *7*(2), 153–164, doi: 10.1002/(sici)1099-1530(199604)7:2<153::aid-ppp215>3.0.co;2-7.

Murton, J. B., and R. K. Belshaw (2011), A conceptual model of valley incision, planation and terrace formation during cold and arid permafrost conditions of Pleistocene southern England, *Quat. Res.*, *75*(2), 385–394, doi:10.1016/j.yqres.2010.10.002.

Musgrave, H., and A. Binley (2011), Revealing the temporal dynamics of subsurface temperature in a wetland using time-lapse geophysics, *J. Hydrol.*, *396*(3–4), 258–266, doi:10.1016/j.jhydrol.2010.11.008.

Nelson, P. H. (1994), Permeability-porosity relationships in sedimentary rocks, *Log Anal.*, *35*(3), 38–62.

Nguyen, F., S. Garambois, D. Jongmans, E. Pirard, and M. H. Loke (2005), Image processing of 2D resistivity data for imaging faults, *J. Appl. Geophys.*, *57*(4), 260–277, doi:10.1016/j.jappgeo.2005.02.001.

Prior, H., and P. J. Johnes (2002), Regulation of surface water quality in a Cretaceous Chalk catchment, UK: An assessment of the relative importance of instream and wetland processes, *Sci. Total Environ.*, *282*, 159–174, doi:10.1016/s0048-9697(01)00950-0.

Pryor, W. A. (1973), Permeability-porosity patterns and variations in some Holocene sand bodies, *Am. Assoc. Pet. Geol. Bull.*, *57*(1), 162–189.

Riddell, E. S., S. A. Lorentz, and D. C. Kotze (2010), A geophysical analysis of hydro-geomorphic controls within a headwater wetland in a granitic landscape, through ERI and IP, *Hydrol. Earth Syst. Sci.*, *14*(8), 1697–1713, doi:10.5194/hess-14-1697-2010.

Shepherd, R. G. (1989), Correlations of permeability and grain-size, *Ground Water*, *27*(5), 633–638, doi:10.1111/j.1745-6584.1989.tb00476.x.

Shevnin, V., A. Mousatov, A. Ryjov, and O. Delgado-Rodriquez (2007), Estimation of clay content in soil based on resistivity modelling and laboratory measurements, *Geophys. Prospect.*, *55*(2), 265–275, doi:10.1111/j.1365-2478.2007.00599.x.

Singha, K., and S. M. Gorelick (2006), Hydrogeophysical tracking of three-dimensional tracer migration: The concept and application of apparent petrophysical relations, *Water Resour. Res.*, *42*, W06422, doi:10.1029/2005WR004568.

Slater, L. D., and A. Reeve (2002), Investigating peatland stratigraphy and hydrogeology using integrated electrical geophysics, *Geophysics*, *67*(2), 365–378, doi:10.1190/1.1468597.

Ward, W. O. C., P. B. Wilkinson, J. E. Chambers, L. S. Oxby, and L. Bai (2014), Distribution-based fuzzy clustering of Electrical Resistivity Tomography images for interface detection, *Geophysical Journal International*, *197*(1), 310–321, doi:10.1093/gji/ggu006.

Wheater, H. S., D. Peach, and A. Binley (2007), Characterising groundwater-dominated lowland catchments: The UK Lowland Catchment Research Programme (LOCAR), *Hydrol. Earth Syst. Sci.*, *11*(1), 108–124, doi:10.5194/hess-11-108-2007.

Wilkinson, P., M. H., Loke, P. I. Meldrum, J. E. Chambers, O. Kuras, D. A. Gunn, and R. D. Ogilvy (2012), Practical aspects of applied optimised survey design for electrical resistivity tomography, *Geophys. J. Int.*, *189*(1), 428–440, doi:10.1111/j.1365-246X.2012.05372.x.

Woods, M. A., and D. T. Aldiss (2004), The stratigraphy of the Chalk Group of the Berkshire Downs, *Proc. Geol. Assoc.*, *115*, 249–265, doi: 10.1016/S0016-7878(04)80006-3.

Younger, P. L. (1989), Devensian periglacial influences on the development of spatially-variable permeability in the Chalk of southeast England, *Q. J. Eng. Geol.*, *22*(4), 343–354, doi:10.1144/gsl.qjeg.1989.022.04.07.

Zedler, J. B. (2000), Progress in wetland restoration ecology, *Trends Ecol. Evol.*, *15*(10), 402–407, doi:10.1016/s0169-5347(00)01959-5.

Zhou, Q. Y., J. Shimada, and A. Sato (2001), Three-dimensional spatial and temporal monitoring of soil water content using electrical resistivity tomography, *Water Resour. Res.*, *37*(2), 273–285, doi:10.1029/2000WR900284.